Monte-Carlo simulation of industrial radiography images and experimental designs

Alice Bonin, B. Chalmond, B Lavayssière

ELSEVIER

NDT&E International 35 (2002) 503–510

NDT&E international

www.elsevier.com/locate/ndteint

Monte-Carlo simulation of industrial radiography images and experimental designs

A. Bonin[a], B. Chalmond[b,*], B. Lavayssière[a]

[a]*Department of Instrumentation, Process and Testing, Electricité de France, R&D Division, France*
[b]*CMLA, Ecole Normale Supérieurede, 61 Avenue du Président Wilson, 94235 Cachan Cedex, France*

Received 27 August 2001; revised 6 February 2002; accepted 12 February 2002

Abstract

In this article, we present a generic software for the simulation of gamma-ray radiography. This software simulates the entire radiographic system, from the source to the detector consisting of metallic screens and films. In an industrial context where the goal is to detect structural flaws in material like cracks, this simulator allows to compute gamma-ray images for different system parameters. By this way, engineers can choose an optimal set of parameters leading to the best image of flaws. We use Monte-Carlo techniques for the simulation of the whole system composed of a source, an object to inspect and a detector. The main contribution of this paper is to show that simulated images are coherent with real images although we use a simplified model for particle transport. Besides, we propose an acceleration technique to simulate the Markov chain of photon transport. Finally, an experimental design is performed leading to a linear model expressing the influence of the system parameters on image quality.

Keywords: Radiographic simulation; Nuclear plant control; Experimental design; Monte-Carlo computation; Argentic film homogenization; Importance sampling

1. Introduction

This article is concerned with industrial radiography applied to the control of nuclear pressurized water reactor vessels. In this context, controlled objects are relatively thick (up to several centimeters). Radiographic controls aim at detecting structural flaws in materials such as cracks. Using iridium or cobalt sources of high energy (up to 1.33 MeV), these controls require exposure times as long as several hours for the thickest objects. This setup implies that engineers must choose the radiographic configuration without the help of on-site experiments. The chosen radiographic configuration is the one that is supposed to give the best image of structural flaws. This paper presents a simulation tool that computes the virtual image corresponding to any chosen radiographic configuration. This software enables engineers to determine the optimal configuration before on-site inspection [4]. Furthermore, this simulation tool is a mean to qualify methods such as tomography algorithms [6].

The framework. We have designed a Monte-Carlo technique to perform the simulation of the *entire radiographic system*. By radiographic system, we mean the association of a source, an object to inspect and a detector composed of a stack of metallic screens and argentic films (Fig. 1). We distinguish between two simulation levels of unequal complexity: in the object (level I) and in the detector (level II). At level I, the simulation technique is well known, but not at level II. The principle of the simulation is to simulate from the source the emission of a very large number of photons (tens of millions for a small image of 5 mm^2) and to follow each of these photons during their interactions within the object and the detector materials. In our context, an interaction can be a Compton or Rayleigh collision which modifies the photon direction, or a photoelectric absorption which causes the photon disappears (Fig. 2). The neglection of the pair production is valid for iridium sources, which are mainly used at EDF, but may impart a bias in the case of a cobalt source.[1] Moreover, during Compton or photoelectric interactions, an electron is emitted. Finally, those emitted electrons are responsible for the radiographic latent image formation when they blacken the grains in the film. At level I, electrons are neglected because their probability to be absorbed before

* Corresponding author. Correspondence address: Cergy-Pontoise University, Physics Department, France. Tel.: +33-147405916; fax: +33-147405901.

E-mail address: bernard.chalmond@cmla.ens-cachan.fr (B. Chalmond).

[1] Referee's remark 2.

0963-8695/02/$ - see front matter
PII: S0963-8695(02)00014-2

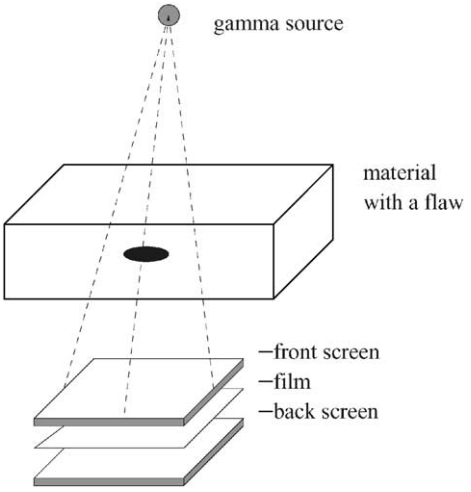

Fig. 1. Radiographic system.

the detector is very high due to the object thickness. Photons transport, i.e. their successive collisions, is simulated by a random walk. However, at level II, electrons are taken into account to simulate the image formation. Here photon and electron transport are modeled by a branching process since each photon can successively generate several electrons during its interactions.

Related works. For fives decades, the particle transport problem at level I has been extensively investigated. This research began with the neutron transport problem for which one provided motivation for applying the Monte-Carlo method [21]. In radiological physics, three kinds of approaches have been adopted. The first one uses Monte-Carlo techniques. Several softwares have been developed in USA (ITS, EGS, MCNP,…) which focus on the simulation of high energy particles but without modeling the particle transport in the detector as in our application [15]. The second one is based on a ray tracing model which is suitable for dealing with arbitrary object geometry contrary to the first approach [8,14]. But, this second approach is only valid for radiographing objects with low energy sources, under the assumption of uniform distribution of scattered radiation. Moreover, the estimation of the distribution of scattered radiation must be performed through several experiments. Several codes have been recently developed: XRSIM [9,12], SINBAD [11], BAMs code [2,22]. The third approach consists in a probability moment expansion for the analytical simulation of the photon scattering problem taking into account regular energy variations. Recent experiments show that the analytical results are in good agreement with the Monte-Carlo results [23]. For our application, we have to radiograph thick objects with high energy sources, and furthermore the radiographic setup must include a detector, and objects and flaws with arbitrary geometry. Monte-Carlo simulation coupled with a CAD description for the geometry is therefore the method of choice for solving our transport problem.

Our contribution. In this context, our aim was to build a simulation tool that simulates images close to reality in acceptable time. Image quality depends on parameters describing the radiographic system configuration: source type, source diameter, source/object distance, object thickness, object material, screen thickness, film type, etc. The main contributions of our paper are (i) the development of a software which simulates images sensible to the physical parameters describing the radiographic configuration, (ii) the design of an acceleration technique for reducing the computing time, (iii) the use of an experimental design technique to summarize the influence of the parameters on image quality.

2. Simulation

Let us first describe the source and the object as it is considered in the software. Sources are gamma sources with spatial extent. To simulate photon emission, we draw uniformly its initial position in the sphere representing the source. The angle a of the emission cone follows the law $p(a) = (\sin a)/(1 - \cos a_{\max})$, and the photon direction is drawn from a uniform distribution on this cone. The photon energy at its emission depends on the source type. For instance, a cobalt 60 source has two equiprobable energy levels (1.17 and 1.33 MeV), and so the energy follows a

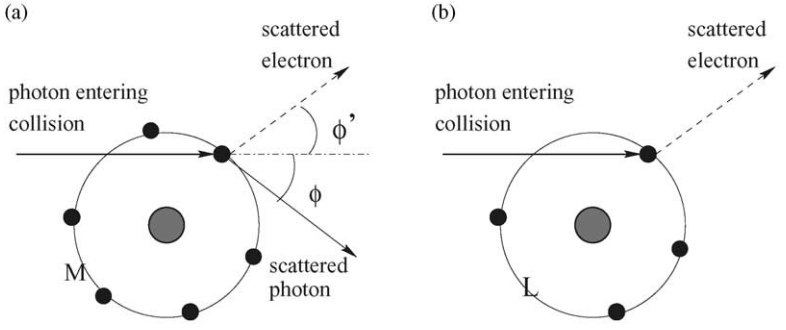

Fig. 2. (a) Compton collision. (b) Photoelectric absorption.

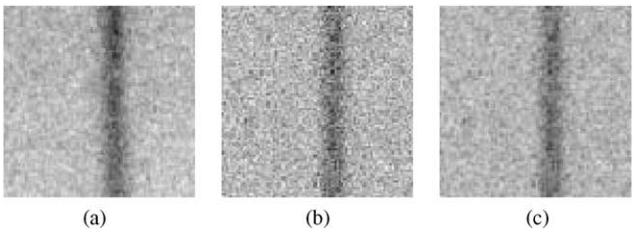

Fig. 3. (a) Real image. (b) Simulated image (with $N = 400$ millions of photons). (c) Image (b) with blur.

Bernoulli law with parameter 0.5. For iridium 192 source, four energy levels must be taken into account.

The object is freely parameterized by the user. Objects are generally made of steel or aluminium, and flaws are represented by steel, aluminium or air inclusions. Though our simulation software enables to simulate images of flaws with complex geometries, we present our results with a parallelipedic electro-eroded notch in a steel object for simplicity purpose. Such a simulated image with an iridium source 390 mm above the object is shown in Fig. 3. The object is 70 mm thick, with a notch of 15 mm depth. The lead front and back screens are 0.2 mm thick. The pixel size is 50 μm. The differences between the three images will be discussed in Section 4. Complex structures like cracks in a casted elbow can also be simulated since the geometry of objects and flaws is described by a boundary representation model or a constructive geometry model. In that case, our code MODERATO is linked to a CAD modeling software [19].

2.1. Simulation in the object

Each photon is emitted by the source with a direction a and an energy λ. Between the source and the object, a photon follows a straight path in the air without energy loss. Once in the object $\mathscr{M}$, a photon encounters several collisions that modify its direction and energy until it escapes from the object or is absorbed by it (Fig. 4). A photon transport is defined by its successive collisions in the object. Following previous works [21,24], we adopt the classical Markov model for this random walk (see Refs. [7,10,16] among many others). Let us denote by $\{Z_n, n \geq 0\}$ this chain, Z_0 being the first collision. $\{Z_n\}$ are random vectors

$$Z_n = (\mathscr{S}_n, \Lambda_n),$$

with states (s_n, λ_n) in $\mathscr{E} = \mathscr{M} \times \mathscr{E} \subset \mathbb{R}^3 \times \mathbb{R}^+$, s_n denoting the position in $\mathscr{M} \subset \mathbb{R}^3$ of the nth collision, and λ_n the photon energy at s_n. The Markovian property means that the photon state, after the nth collision, is completely determined by a conditional probability distribution depending only on the previous state z_{n-1}. Then the Markov chain is entirely defined by its transition probabilities.

Markovian formulation. Let us consider the nth random collision $Z_n = (\mathscr{S}_n, \Lambda_n)$, as shown in Fig. 5. Three random events are likely to occur: photoelectric absorption (*Phot*), Compton diffusion (*Comp*) or Rayleigh diffusion (*Rayl*). Let us denote by C_n the discrete random variable with values {Phot, Comp, Rayl}. Its probability distribution $\pi_0(C_n = c|\lambda_{n-1})$ only depends on the incident photon energy and the atomic number of the material. The direction a_n of a photon after Compton or Rayleigh collisions follows a well-known probability distribution, as does the distance L_n between s_n and s_{n+1}. Let us write:

$$a_n = \frac{s_{n+1} - s_n}{\|s_{n+1} - s_n\|}, \qquad \ell_n = \|s_{n+1} - s_n\|,$$

Instead of $z_n = (s_n, \lambda_n)$ we will use:

$$z_n = (a_n, \ell_n, \lambda_n).$$

Since (a_n, L_n) defines s_n, we continue to denote by z_n the states (a_n, L_n, λ_n). The transition kernel $\mathrm{d}K$ defines the probability distribution of Z_n conditionally to the previous state z_{n-1}

$$\begin{aligned}\mathrm{d}K(z_{n-1}; z_n) &= \sum_c \pi(z_n|z_{n-1}, C_n = c)\pi_0(C_n = c|\lambda_{n-1}) \\ &= \sum_c \pi_1(a_n|z_{n-1}, C_n = c) \\ &\quad \times \pi_2(\ell_n, \lambda_n|a_n, z_{n-1}, C_n = c)\pi_0(C_n = c|\lambda_{n-1}),\end{aligned} \tag{1}$$

where these lines follow the Bayes' formula. We derive from the particle physics laws, the expression of π_1 and π_2 [24]. For a Compton collision, π_1 is the Klein–Nishina law denoted *KN*. The Rayleigh diffusion is governed by a

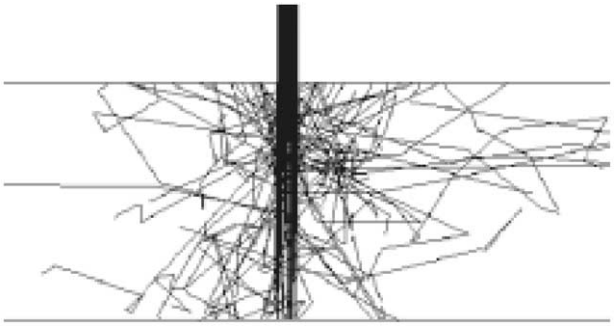

Fig. 4. Photons trajectories.

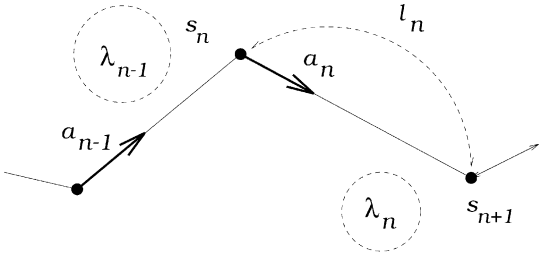

Fig. 5. Collision parameters for the photon transport model.

law denoted R, derived from KN. These laws describe the deviation $\phi_n = a_n - a_{n-1}$:

$$\pi_1(a_n|z_{n-1}, C_n = \text{Comp}) = \text{KN}((a_n - a_{n-1}), \lambda_{n-1}),$$

$$\pi_1(a_n|z_{n-1}, C_n = \text{Rayl}) = R(a_n - a_{n-1}).$$

R does not depend on the energy. For $c \in \{\text{Comp}, \text{Rayl}\}$, π_2 is an exponential law $\mathscr{E}(\mu(\lambda_n))$[2]

$$\pi_2(\ell_n, \lambda_n|a_n, z_{n-1}, C_n = c) \propto \mu(\lambda_n)\mathrm{e}^{-\mu(\lambda_n)\ell_n} \times \mathbf{1}[\lambda_n = \hbar(\lambda_{n-1}, a_n - a_{n-1})],$$

where μ is the so-called attenuation function and $\hbar$ is a determinist function giving the photon energy after a collision:[3]

$$\hbar(\lambda, \phi) = \frac{\lambda}{1 + \kappa\lambda(1 - \cos\phi)}. \quad (2)$$

Simulation process. For every photon emitted by the source, the software simulates its random walk by successive simulations. At the nth collision, the collision type c is drawn according to $\pi_0(C_n = c|\lambda_{n-1})$

$$\pi_0(c|\lambda) = \frac{\sigma_c(\lambda)}{\sigma_{\text{Comp}}(\lambda) + \sigma_{\text{Rayl}}(\lambda) + \sigma_{\text{Phot}}(\lambda)}, \quad (3)$$

where σ_c depends on the material type. The interested reader can find these 'cross-section' values, for example, in tables [13]. These coefficients also define the attenuation function

$$\mu(\lambda) \propto \sigma_{\text{Comp}}(\lambda) + \sigma_{\text{Rayl}}(\lambda) + \sigma_{\text{Phot}}(\lambda),$$

where the constant of proportionality is a characteristic of the material. Let us note that the simulation algorithm must take into account the case when a photon crosses a flaw, which is not explicit in the expression of π_2.

We now present the simulation process for level I which is a classical process. At the nth step of the random walk, the simulation software draws the collision type according to Eq. (3). If $c = \text{Phot}$ then the walk terminates. If $c = \text{Comp}$, then ϕ_n and L_n are, respectively, drawn according to KN and π_2 while λ_n is computed by Eq. (2). Similarly, if $c = \text{Rayl}$ then ϕ_n and ℓ_n are drawn according to R and π_2 while the energy remains unchanged. With source energies used for our controls (from 0.3 to 1.33 MeV), Compton interaction is predominant. But while a photon loses energy during its successive collisions, Rayleigh and photoelectric absorption become more and more probable. By simulating a very large number N of random walks, we obtain a 'virtual image' behind the object. This image is obtained by counting on a regular grid $\mathscr{G}$ the number of photons in each cell.

Variance reduction. In Annex, we propose a new technique to reduce N without degrading image quality. The reduction rate is around 30%. This technique belongs to the family of 'importance sampling' techniques [10]. It consists in modifying the transition kernel so that photons are more likely to reach the detector. Indeed, in most of our radiographic setup with the natural Markov chain, around 70% of photons do not reach the detector (Fig. 4). This occurs either because photons are absorbed or because they exit from the object outside the detector. Modifying the transition kernel alleviates this drawback.

2.2. Simulation in the detector

Our software deals with the usual radiographic detector consisting in a stack of films and screens. To simplify our presentation we suppose that the detector only contains a film between a front screen and a back screen (Fig. 1). Particle transport in the detector (level II) is more complex than in the object since photons participate to the image formation through the electrons that are emitted during the photon collisions. A film is composed of at least one emulsion layer of gelatin containing silver halide grains on a film base. As particles do not encounter interactions in the film base that contribute to the image formation, we make the simplifying assumption of a film consisting of gelatin containing silver halide grains with uniform spatial repartition. Then, the film thickness is the sum of the gelatin layer thicknesses. Note that the film base can be easily truly modelized if cross-section tables are available for the material. In our experiments, the film is 40 μm thick with mean grain density of 10^9 grains/mm^3 and mean grain diameter of 0.7 μm. Particle transport is summarized on Fig. 6. It can be seen as a branching process [1], because a single photon can successively liberate several electrons. Once liberated, an electron has a straight trajectory along which it crosses all the grains situated on it.

We assume that a grain is blackened as soon as an electron reaches it. Let us emphasize that this electron transport

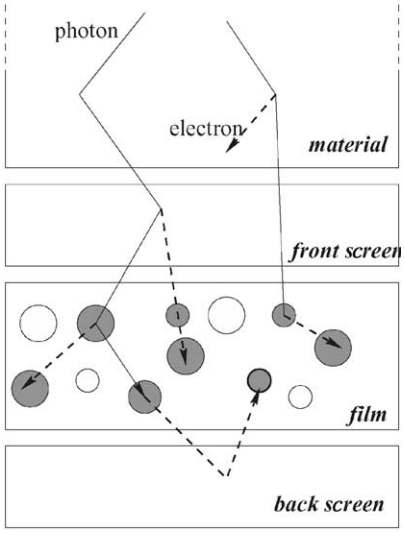

Fig. 6. Particle transport in the detector (—photon trajectory, - - -electron trajectory).

[2] $\mathbf{1}[A]$ is the indicator function: $\mathbf{1}[A] = 1$ if A is true and 0 otherwise.
[3] κ is a constant: it is the inverse of the electron energy at the rest.

simplification enables the software to generate realistic images in acceptable time. In the film, an electron blackens all the grains that it crosses along its trajectory. Each photon of the virtual image obtained at level I generates such a branching process. Finally, the latent image is obtained by counting on a regular grid the number of blackened grains in each cell.

Homogenization. To simulate the branching process in the film, an obvious approach would be to simulate a repartition of spherical grains with random radii and then to simulate the branching process through this spatial configuration. This would be extremely time and memory consuming due to the large number of grains. This is why we have adopted an 'homogenization' approach that we present in the following.

The mean number of grains by volume unit is very high for commonly used films so that a 5 mm^2 film contains several billions of grains. Manufacturers try to obtain a homogeneous repartition for grains and we can assume that the grain repartition is uniform. This is why we consider the film as a homogeneous material which will be later characterized by two parameters: ϵ_g, the mean distance between two grains and τ_g, the mean grain diameter. Thus the detector is composed of three homogeneous materials: two screens and a film. Then the photon transport in these materials is similar to the one in the object, the cross-section coefficients being those of the grains.

Electron transport. After the Compton collision of a photon with energy λ, the emitted electron has energy λ' and deviation angle ϕ' satisfying (cf. Fig. 2 and Ref. [17]

$$\lambda' = \lambda \frac{\kappa\lambda(1-\cos\phi)}{1+\kappa\lambda(1-\cos\phi)}, \qquad \phi' = \arctan\frac{1}{(1+\kappa\lambda)\tan(1/\phi)}, \tag{4}$$

where ϕ is the photon deviation angle. The mean free path of the electron is defined in Ref. [20]

$$\mathcal{L}' = \frac{0.407}{r}\lambda'^{1.38} \text{ if } \lambda' < 0.8 \text{ MeV} = \frac{1}{r}(0.542\lambda' - 0.133) \text{ if } \lambda' > 0.8 \text{ MeV}, \tag{5}$$

r being the volumic density of the material.

In the screens, only electrons diffused towards the film contribute to the image formation, so only back-scattered electrons are useful in the back-screen (the front screen plays a reinforcing role as it liberates numerous electrons that will reach the film because of the low screen thickness). In the back screen, back-scattering predominates and we model it directly. For an electron, the probability to be back-scattered is determined thanks to dedicated cross-sections, and the back-scattering angle ϕ' follows the Rutherford's law [5]. We now describe the particle transport in the film.

Simulation process. The film (gelatin and grains) being considered as a homogeneous material, photons collisions are simulated according to the simulation process described in Section 2.1. Then, given these collisions, we have to simulate the electron trajectories across the grains although they are not explicitly present in the homogenized film. Because of the simplification made earlier, for every electron we can assume that the positions where it hits a grain along its trajectory, are distributed as the grain positions along this trajectory. Consequently, this distribution can be described by a model with parameters ϵ_g and τ_g. To do that, we decompose the length trajectory as

$$\mathcal{L}' = \sum_{i=1}^{I} \mathcal{L}'_i, \qquad \text{with } \mathcal{L}'_i = \tau + \epsilon, \tag{6}$$

where $\mathcal{L}'_i$ is the distance between two collisions occurred within two neighboring grains (we assume that only one collision can occur in a grain). The collision number I depends on the electron energy. ϵ is the random distance between two neighboring grains and τ is the random length of the electron path in both grains. We suppose that $\mathcal{L}'_i$ follows an exponential law $\mathcal{E}((\tau_g + \epsilon_g)^{-1})$ whose expectation is $\mathbb{E}(\mathcal{L}'_i) = \tau_g + \epsilon_g$. To simulate an electron trajectory, the algorithm computes $\mathcal{L}'$ by Eq. (5) and then draws successively $\mathcal{L}'_i$ according to the exponential law under the constraint (6). After each collision i, the electron loses a part of its energy as it can be computed by inverting Eq. (5).

3. Experimental results and optimization

In Section 1, we have mentioned that the radiographic image quality depends on the choice of the radiographic setup: source type, source diameter, film type, front and back screen thickness, source/object distance, and on the object parameters: thickness, inclusion position, material type, etc. We try now with our simulation software to understand the influence of these parameters on the image quality y measured in terms of contrast and blur in the case of parallelipedic inclusions. The contrast is the gray level difference between the inside and outside of the flaw in the simulated image. The blur is the measured line spread function of the flaw edge. It means that we are able to extract such values from every image.

Experimental design methodology is a well suited technique to analyze and optimize the influence of parameters (also called factors) (cf. Ref. [18] among many others). We have identified eight main factors. For sake of clarity, we restrict our presentation to three factors with two modalities: source diameter (0.1 mm, 3 mm), front screen thickness (low, standard), back screen thickness (low, standard). These factors are, respectively, denoted by A, B, C and are coded by $\{-1,1\}$. To observe all factor combinations we need to perform 2^3 experiences, that is eight simulations. Fig. 7 shows simulated images corresponding to six combinations in the same radiographic setup as Fig. 3.

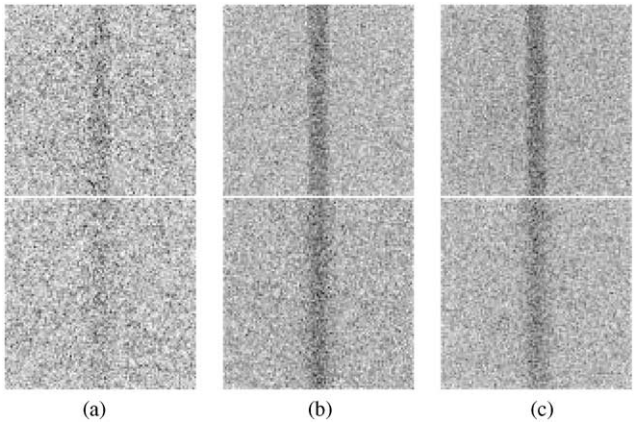

Fig. 7. Simulated images (with $N = 400$ millions of photons) from a two-level factorial design 2^3, the factors being: $A =$ source diameter, $B =$ front screen thickness, $C =$ back screen thickness. For the first line: $A = 0.1$ mm and for the second line: $A = 3$ mm. For each line, the factor modalities correspond to: (a) film 'alone', (b) film with front screen, (c) film with front screen and back screen.

The results of these simulations respect the expert knowledge. Without screen of significant thickness, the radiographic image has a very poor quality whatever the source size: 0.1 mm (Fig. 7(a)/line 1) or 3 mm (Fig. 7(a)/line 2). The main qualitative effect is due to the front screen factor B (Fig. 7(b)). Given B, the source factor A has major influence but the back screen factor C has a minor one.

This experimental design can be more deeply analyzed by statistical techniques [18]. If we consider that the image quality measure y is the occurrence of a random variable Y, this analysis is based on a linear model which gives a decomposition of the expectation $\mathbb{E}(Y)$. For each triplet $(a,b,c) \in \{-1,1\}^3$, this expectation is denoted by $\mathbb{E}(Y) = \tau(a,b,c)$, and the model reads as

$$\tau(a,b,c) = \bar{e} + a\,e_A(a) + b\,e_B(b) + c\,e_C(c) + ab\,e_{AB}(a,b) + ac\,e_{AC}(a,c) + bc\,e_{BC}(b,c) + abc\,e_{ABC}(a,b,c),$$

where e_A, e_B and e_C are the main effects, $e_{AB},\ldots,e_{ABC}$ are the interaction effects and $\bar{e}$ is the mean effect. This model naturally assumes that: $\sum_a e_A(a) = 0,\ldots,\sum_b e_{AB}(a,b) \times = \sum_b e_{AB}(a,b) = 0,\ldots$ The statistical analysis of the eight y values extracted from the simulated images confirms that first, B and second, A are the main principal effects. Furthermore, A has a slight influence through the interaction AB. On this limited experimental design, the effect of C is not statistically significant. So, the model is reduced to:

$$\tau(a,b,c) = \bar{e} + a\,e_A(a) + b\,e_B(b) + ab\,e_{AB}(a,b). \quad (7)$$

For instance, the triplet $(1,-1,1)$ gives:

$$\tau(1,-1,1) = \bar{e} + e_A(1) - e_B(-1) - e_{AB}(1,-1).$$

For this linear model, the effects are estimated by minimizing the least-square criteria between y and τ.

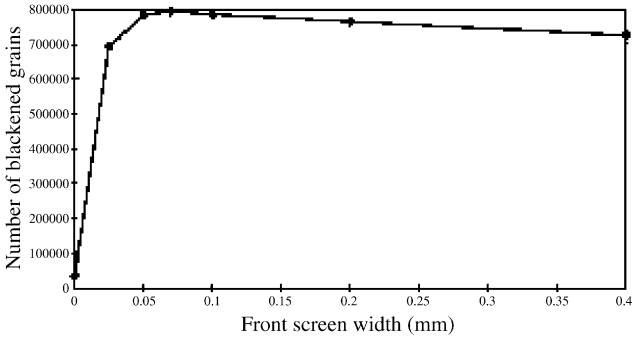

Fig. 8. Image density versus front screen thickness.

Surprisingly, the simulation software is able to reproduce fine effects that we observe on real radiographic images. For instance, using our simulation software, we have obtained an image density curve in terms of the factor B (front screen thickness). This curve is coherent with the real experiments (Fig. 8).

Thus, we determine that the optimal front screen thickness is 0.75 mm, which is exactly what real experiments give for this configuration. In this context we can try to optimize the system parameters by handling more than one factor, for instance A and B. Such a problem can be solved by using a model similar to Eq. (7) but with quantitative variables A and B instead of binary ones. It is the well-known surface response technique where one tries to optimize the system response y in terms of a and b, [18]. Let us add that the computation of a simulation without importance sampling, and using 100 million of photons for a 5 mm^2 film digitized on a 100^2 grid takes less than one hour on a Pentium III 650.

4. Conclusion

We have presented a simulation tool for representing the radiographic process from the source to the detector. The particle transport simplification and the Markov chain simulation acceleration lead to acceptable computation times in the industrial context of non-destructive evaluation. This simulation tool is highly configurable and simulated images are sensitive to parameter modification in the same way as real images. Besides, the experimental design through surface response methodology and the resulting model is of great interest for experts to assist them in their analytical approach of radiography.

The qualities of this simulation software must, however, be tempered by the fact that the film development process is not modelized. This leads to a difference between real and simulated images as shown on Fig. 3. Development seems to introduce an additional blur. We work on estimating this blur through a point spread function estimated from the comparison of real and simulated images. Fig. 3(c) shows the introduction of such a blur. However, this blur does not

modify the relative influence of parameters on the radiographic images, and consequently it is not a drawback for factor analysis.

5. Annex: variance reduction

Following Ref. [7], the two next sections recall the classical framework for achieving variance reduction using *importance sampling technique*. To gain an advantage, most successful applications of the method rely on exploiting the peculiarities of the particular problem at hand. In the third section, we propose a original and generic approach to determine specific laws for importance sampling.

Natural Markov chain. Let us assume that the grid $\mathscr{G}$ is composed of elementary cubes v and that the range of energy is partitioned into intervals $\bar{\lambda}$ of center λ. For every $\mathscr{V} = (v, \bar{\lambda})$, we have to estimate the probability $Q(z_0) = \text{Prob}(z_0; \mathscr{V})$ that a photon reaches $\mathscr{V}$ from its initial state z_0. This probability is written:

$$Q(z_0) = \sum_{j=0}^{\infty} P_j(z_0)$$

where $P_j(z_0)$ is the probability that a photon reaches $\mathscr{V}$ from the state z_0 after j and only j collisions in $\mathscr{M}$ after z_0:

$$P_j(z_0) = P[Z_{j+1} \in \mathscr{V}, Z_j \notin \mathscr{V} | Z_0 = z_0].$$

Let us truncate this series:

$$Q(z_0) \approx \sum_{j=0}^{J} P_j(z_0).$$

The estimate of $Q(z_0)$ will be of the form:

$$\hat{Q}(z_0) = \sum_{j=0}^{J} \hat{P}_j(z_0).$$

Let us detail how the estimate $\hat{P}_j(z_0)$ is obtained. Let $\{z_n^{(i)}, 0 < n \leq J+1\}_{i=1,\ldots,m}$ be m independent occurrences of the Markov chain $\{Z_n, 0 < n \leq J+1\}$ with kernel $K(z_0; \cdot)$. By noting that

$$P_j(z_0) = \int_{(z_1,\ldots,z_{j+1}) \in E^{j+1}} \left[\prod_{n=1}^{j+1} \mathrm{d}K(z_{n-1}; z_n) \right] \mathbf{1}[s_j \in \mathscr{M}, s_{j+1} \in v] \mathbf{1}[\lambda_{j+1} \in \bar{\lambda}]$$

$$= \mathbb{E}_{K_{(z_0;\cdot)}^{(j+1)}}[\mathbf{1}[\mathscr{S}_j \in \mathscr{M}, \mathscr{S}_{j+1} \in v]],$$

we are lead to consider the following estimator:

$$\hat{P}_j(z_0) = \frac{1}{m} \sum_{i=1}^{m} \mathbf{1}[\mathscr{S}_j^{(i)} \in \mathscr{M}, \mathscr{S}_{j+1}^{(i)} \in v] \mathbf{1}[\Lambda_{j+1}^{(i)} \in \bar{\lambda}].$$

This estimator is justified by the law of large number and by the fact that it is unbiased: $\mathbb{E}_{K_{(z_0;\cdot)}^{(j+1)}}[\hat{P}_j(z_0)] = P_j(z_0)$.

Biased Markov chain. To reduce the computation time, we do not use anymore the natural Markov chain but a new Markov chain with kernel $\tilde{K}$ for which the associated estimator $\tilde{P}_j(z_0)$ has an equivalent accuracy, but for a smaller number of occurrences ($\tilde{m} < m$). In the literature, this procedure is called 'importance sampling'. So, let $\{z_n^{(i)}, 0 < n \leq J+1\}_{i=1,\ldots\tilde{m}}$ be $\tilde{m}$ independent occurrences of the Markov chain $\{Z_n, 0 < n \leq J\}$ with kernel $\tilde{K}$. The new estimator is:

$$\tilde{P}_j(z_0) = \frac{1}{\tilde{m}} \sum_{i=1}^{\tilde{m}} \left[\prod_{n=1}^{j+1} \frac{\mathrm{d}K(Z_{n-1}^{(i)}; Z_n^{(i)})}{\mathrm{d}\tilde{K}(Z_{n-1}^{(i)}; Z_n^{(i)})} \right]$$

$$\times \mathbf{1}[\mathscr{S}_j^{(i)} \in \mathscr{M}, \mathscr{S}_{j+1}^{(i)} \in v] \mathbf{1}[\Lambda_{j+1}^{(i)} \in \bar{\lambda}]$$

$$= \frac{1}{\tilde{m}} \sum_{i=1}^{\tilde{m}} \Psi_j^{(i)} \mathbf{1}[\mathscr{S}_j^{(i)} \in \mathscr{M}, \mathscr{S}_{j+1}^{(i)} \in v] \mathbf{1}[\Lambda_{j+1}^{(i)} \in \bar{\lambda}].$$

Clearly, this is an unbiased estimator: $\mathbb{E}_{\tilde{K}_{(z_0;\cdot)}^{(j+1)}}[\tilde{P}_j(z_0)] = P_j(z_0)$. This property is due to the weight $\Psi_j^{(i)}$.

Biased kernel estimation. The importance sampling technique consists in replacing the natural laws π_0, π_1 and π_2 which define the kernel K by new ones in order to define the biased kernel $\tilde{K}$. Let us present our original approach for the deviation law in the case of Compton collision.

To do that, let us consider m_0 independent occurrences of the natural Markov chain, with $m_0 \ll \tilde{m}$. Let $D = \{(\phi_i, \lambda_i); i = 1, \ldots, m_0'\}$ be the set of deviations and energies obtained during the simulation of these occurrences (we have $m_0 < m_0'$ since there are at least one collision per photon). For every λ, this set gives a sample of the random variable $(\Phi|\lambda)$ of law $\text{KN}(\phi, \lambda)$. Now, let $\tilde{D}$ be the restriction of D to the occurrences having reached the grid $\mathscr{G}$. For every λ, $\tilde{D}$ gives a sample of the biased law $\widetilde{KN}$, which contributes to define $\tilde{K}$. Practically, we choose a parametric expression $\widetilde{KN}_\alpha$ for $\widetilde{KN}$, and then, the biased law is *estimated* according to the pseudo maximum likelihood principle [3]. By setting $\tilde{D}_{\bar{\lambda}} = \{(\phi_i, \lambda_i) : \lambda_i \in \bar{\lambda}\}$, for every $\bar{\lambda}$, we compute the pseudo maximum likelihood estimate of α:

$$\hat{\alpha}_{\bar{\lambda}} = \arg \max_{\alpha} \prod_{(\phi_i,\lambda_i) \in \tilde{D}_{\bar{\lambda}}} \widetilde{\text{KN}}_\alpha(\phi_i \lambda_i).$$

Acknowledgements

This work was supported by SUDIMAGE S.A., R&D group, under a Cifre grant.

References

[1] Asmussen A, Hering H. Branching processes. Basel: Birkhauser, 1983.
[2] Bellon C, Tillack GR, Nockemann C, Stenzel L. Computer simulation of X-ray NDE process coupled with CAD interface. Rev Prog Quantitative Non Destruct Eval 1995;16.
[3] Besag J. Spatial interaction and the statistical analysis of lattice systems. J R Stat Soc 1974;B-36:192–236.
[4] Bonin A, Chalmond B. Moderato: a monte carlo radiographic simulation. Rev Prog Quantitative Non Destruct Eval 1999;19.

[5] Cauchois Y, Héno Y. Cheminement des particules chargés. Paris: Gauthier Villars, 1964.
[6] Chalmond B, Coldefy F, Lavayssière B. Tomographic reconstruction from non-calibrated noisy projections in non-destructive evaluation. Inverse Probl 1999;15:399–411.
[7] Chalmond B. Modeling for image analysis. Berlin: Springer, 2000 in French.
[8] Della Rocca A, Ferriani S, La Porta L. Computer simulation of the radiographic image formatting process: implementation and applications. NDT&E Int 1995;28(3):7163–70.
[9] Elshafiey I, Gray JN. Optimization tool for X-ray radiographic NDE. Rev Prog Quantitative Non Destruct Eval 1996;15 New York.
[10] Fishman GS. Monte Carlo. Berlin: Springer, 1995.
[11] Glière A. Sindbad: from CAD model to synthetic radiographs. Rev Prog Quantitative Non Destruct Eval 1998;17 New York.
[12] Gray JN, Inanc F, Shull BE. Three dimensional modeling of projection radiography. Rev Prog Quantitative Non Destruct Eval 1989;8A.
[13] Hubbell JH. Photon cross sections, attenuation coefficients and energy absorption coefficients from 10 to 100 GeV. National Bureau of Standards NSRDR-NBS 1969;29 Washington.
[14] Inanc F. Analysis of X-ray and gamma ray scattering through computational experiments. J Nondestruct Eval 1999;18(2).
[15] Jenkins TM. Monte Carlo transport of electrons and photons. New York: Plenum Press, 1988.
[16] Lapeyre B, Pardoux E, Sentis R. Monte-Carlo techniques for transport equation and diffusion. Berlin: Springer, 1998 in French.
[17] Leo WR. Techniques for nuclear and particle physics experiments: a how-to approach. 2nd ed. Berlin: Springer, 1994.
[18] Myers R, Montgomery D. Response surface methodology: process and product optimization using designed experiments. New York: Wiley, 1995.
[19] Schumm A. Ultrasonic ray models for complex geometries, Rev Prog QNDE, vol. 19. New York: Plenum Press, 1997.
[20] Segré E. Nuclei and particles. 2nd ed 1977.
[21] Spanier J, Gelbard EM. Monte Carlo principles and neutron transport problem. Reading, MA: Addison-Wesley, 1969.
[22] Tillack GR, Bellon C, Artemiev V, Naumov AO. Simulation of scattering process in radiation techniques exploiting the theory of Markovian processes with random structure. Rev Prog Quantitative Non Destruct Eval 1997:16.
[23] Tillack GR, Arteniev VM, Naumov AO. Statistical linearization method for analytical simulation in nonhomogeneous media. Bundesanstalt fur Materialforschung. Research Report, May 1997.
[24] Williamson FF. Monte-Carlo simulation of photon transport phenomena: sampling techniques. In: Morin RL, editor. Monte-Carlo simulation in the radiological sciences, Boca Raton: CRC Press, 1988. p. 53–101.